Received: 7 May 2022 | Revised: 22 June 2022 | Accepted: 14 July 2022

DOI: 10.1111/jace.18681

Journal of the American Ceramic Society

RESEARCH ARTICLE

A new self-consistent empirical potential model for multicomponent borate and borosilicate glasses

Marco Bertani | **Annalisa Pallini** | **Marina Cocchi** | **Maria Cristina Menziani** | **Alfonso Pedone**

Department of Chemical and Geological Sciences, University of Modena and Reggio Emilia, Modena, Modena, Italy

Correspondence
Alfonso Pedone, Department of Chemical and Geological Sciences, University of Modena and Reggio Emilia, Via G. Campi 103, 41125 Modena, MO, Italy.
Email: alfonso.pedone@unimore.it

Abstract

A new self-consistent empirical potential model based on the BMP potential [Bertani et al., Phys. Rev. Mat. 5 (2021) 045602] has been developed for the simulation of multicomponent borate and borosilicate glasses. We exploited the Bayesian optimization approach to create a set of parameters for the B–O interaction, which depends on the glass composition, and in particular on the $R = ([A_2O]+[AEO])/[B_2O_3]$ (A = alkaline and AE alkaline-earth ions) and $K = [SiO_2]/[B_2O_3]$ ratios. The obtained force field (FF) has been applied to several borate and borosilicate glass series containing, as modifier oxide, Na_2O, Li_2O, CaO, and MgO and tested on experimental data, such as the fraction of BO_4 (N_4), density, non-bridging oxygen speciation, neutron diffraction spectra, ^{11}B, ^{29}Si, and ^{17}O magic angle spinning nuclear magnetic resonance. A comparison with other interatomic potentials available in literature has also been performed. The results show that the FF reproduces well almost all the abovementioned properties, showing excellent agreement with experimental data in a wide range of compositions.

KEYWORDS
molecular dynamics, structure, borates, borosilicate glass

1 | INTRODUCTION

Multicomponent borates and borosilicate glasses find many technological applications in several fields.[1,2] They are used to make kitchen and laboratory glassware, optical glass fibers, protective cover glasses, and glass substrates for high-performance electronic displays,[3,4] bioactive glasses used in orthopedic and dentistry, as soft tissue healing materials in human biomedicine,[5–7] and matrices for the safe immobilization of nuclear waste.[8,9]

Although there has been an upsurge in the development of borate- and borosilicate-based glasses, the majority of the glasses reported in the literature have been designed using the conventional "trial-and-error" approach because of the lack of a detailed understanding of the composition–property relationships in these glasses. The determination of such relationships relies on the detailed knowledge of the atomic level structure of these glasses, which is, however, challenging because of the amorphous nature and the wide range of local and medium-range structural features

encountered in multicomponent oxide glasses. Classical molecular dynamics (MD) simulations are playing a key role in studying the structure and properties of glasses because, thanks to their low computational cost, they allow the investigation of large systems (containing up to 10^6 atoms) for long times (up to ms).[10]

However, MD simulations are limited by the availability of accurate and transferable empirical potentials, or force fields (FFs). This is a critical issue particularly for borates and borosilicate glasses because the development of B–O interatomic potentials able to reproduce boron environment in multicomponent glasses in a wide compositional space is hampered by the complex chemistry of boron in glasses.

Indeed, unlike silicon (always present as SiO_4 tetrahedra in silicate glasses), boron is found in tetrahedral or triangular structures (BO_4 and BO_3 units, respectively) depending on glass composition and thermal history.[11–15]

The structure of vitreous B_2O_3 is understood as interconnected BO_3 units through the so-called bridging oxygens (BOs) to form three-membered rings (boroxol rings) connected by B–O–B bridging bonds of 135° wide.[16,17]

The addition of alkaline oxides (M_2O) causes two possible phenomena: (i) the breakage of the B–O–B bond and the formation of non-BOs (NBOs) as in silicates, following the equation $1/2M_2O + B\text{Ø}_3 = M^+ + B\text{O}\text{Ø}_2^-$ where Ø represents BO atoms that are shared between adjacent (super)structural borate units, or (ii) the conversion of BO_3 units to BO_4 units, following the equation $1/2M_2O + B\text{Ø}_3 = M^+ + B\text{Ø}_4^-$. In the first case, the alkaline cations act as modifiers, whereas in the second one, they act as charge compensators of the BO_4^- units. Nuclear magnetic resonance (NMR)[15] and RAMAN[13,18,19,15,20,21] experiments suggest that the second mechanism is dominant when the ratio $R = [M_2O]/[B_2O_3] < 0.5$, whereas both mechanisms coexist for higher ratios.

A comprehensive structural model of sodium borate glasses was proposed by Dell and Bray[15,20] on the basis of ^{11}B NMR data.[15,20,21] In this model, the variation of boron coordination with composition is rationalized on the basis of the parameters $R = [Na_2O]/[B_2O_3]$, as displayed by the black curve in Figure 1. At low R, each Na^+ cation acts as a charge compensator, and the BO_4 fraction (also denoted as N_4) increases linearly with R until $R_{max} = 0.5$. Further addition of sodium oxide leads to the formation of NBO on BO_3 units and at the consequent conversion of BO_4 in BO_3, as the negative-charged BO_4 disfavors the formation of NBO atoms on this species. For this reason, the N_4 fraction decreases progressively until no BO_4 is present at $R > 2$.

Similar behavior is observed for borosilicate glasses. However, as shown in Figure 1, in these systems, the N_4 fraction depends also on the value of $K = [SiO_2]/[B_2O_3]$.

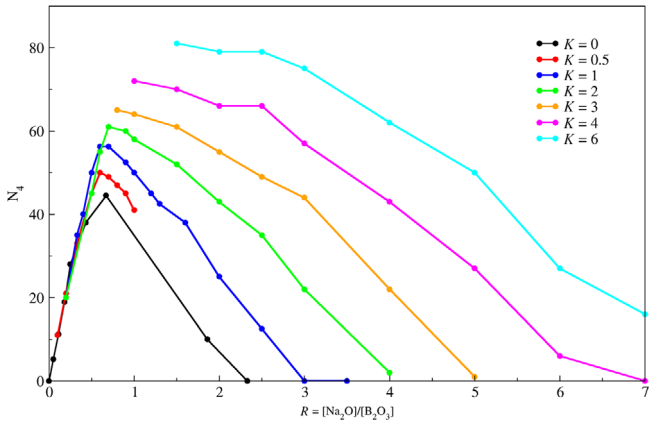

FIGURE 1 Graphical representation of the dependence of the N_4 fraction in borosilicate (black curve) and sodium borate (colored curves) glasses as a function of $R = [Na_2O]/[B_2O_3]$ and $K = [SiO_2]/[B_2O_3]$. The graph is based on experimental data.[15,20,21]

At constant K value, the N_4 fraction increases up to $R_{max} = (K/8 + 1)/2$, then a plateau is observed between R_{max} and $R_D = (K/2 + 1)/2$ meaning that further addition of modifiers creates NBOs on silicon. After R_D, a further addition of Na_2O forms NBOs on trigonal BO_3 species, thus reducing N_4. Note that the relative BO_4 population grows with the SiO_2 content of the borosilicate glass, and that the maximum amount of it is consistently higher than the corresponding borate analogs ($K = 0$).

This peculiar and complex behavior of boron leads to a nonlinear variation of glass chemical properties (called boron anomaly), which is precious for the industry that widely exploited it to produce high-tech glasses, but it is a huge bottleneck for the development of reliable empirical FFs.

Indeed, the earlier MD simulations of sodium borosilicate glasses were carried out using the Born–Mayer–Huggins two-body interatomic potentials with formal charges and yielded N_4 values in qualitative agreement with experimental data.[17,22,23] A better agreement was obtained with the interatomic potential introduced by Kieu et al.[24] and Inoue et al.,[25] which allowed reproducing the variations in the coordination number of borate units as a function of composition, owing to the direct dependence of atomic charges and boron parameters on glass composition. However, there are several shortcomings in these potentials; the main one is their low transferability to multicomponent glasses.

In the past 4 years, new interatomic potentials parameters were developed by Wang et al.,[26] (hereafter referred to as Bauchy potential); Deng and Du,[27] (Du potential); Sundararaman et al.[28,29] (SHIK potential, from the authors' names Sundararaman, Huang, Ispas, and Kob); Stevensson et al.[30] (Stevensson–Edèn potential); and by Pacaud

et al.[31] These have been validated on neutron diffraction and N_4 values determined by NMR experiments on borates and borosilicate glasses, in different compositional spaces.

The first three potentials are based on the rigid ionic model with partial charges and pair-wise (Buckingham) interatomic potentials for short-range interactions.

On the contrary, the potentials developed by Stevensson–Edén and Pacaud are polarizable FFs. In particular, Stevensson–Edén's potentials are based on the shell model proposed by Dick and Overhauser,[32] where the total charge Z of the oxygen ions is split between a massive core (of charge $Z+Y$) and a massless shell (of charge $-Y$) which are coupled by a harmonic spring. Instead, the Pacaud potentials are based on the polarizable ion model developed by Madden et al.,[33] in which at each ion a dipole polarizability and an induced dipole moment (determined by minimizing the polarization energy term) are associated.

It is worth highlighting that the Bauchy, Stevensson–Edén, and Pacaud potentials are independent on glass compositions, whereas Du and SHIK potentials depend on glass compositions. In particular, in the Du potential, the Buckingham parameter A_{ij} of the B–O interaction depends on the composition and on the percentage of N_4 species in the glass expected by the YDBX model,[15] whereas in the SHIK potential, the partial charge of oxygen depends on the composition.

In recent works,[34,35] Bauchy, Du, and Stevensson–Edèn potentials have been evaluated in the reproduction of the short-to-medium range structure of some sodium borosilicate glasses in several R and K regions. The results of these works showed that, concerning the rigid-ion force-fields, the Bauchy potential can reliably reproduce the partitioning between BO_3 and BO_4 species at values of $R < 1$, whereas at higher R values, it shows an opposite trend compared to the experiment. Instead, the Du potentials can reproduce the N_4 fraction for all the R-values, thanks to its variable parameters. As for the Stevensson–Edén potential, it underestimates N_4 in glasses with $K < 0.33$ but can accurately reproduce the ^{11}B and ^{29}Si magic angle spinning (MAS)–NMR spectra of glasses with higher K-values due to the formation of a few three-membered rings (not observed with the rigid ionic models) in the glass and the narrower T–O–T bond angle distributions (BADs).

In this work, the BMP force-field[36,37] (from author surnames Bertani–Menziani–Pedone), a potential recently developed by some of us as the evolution of the PMMCS[38,39] (Pedone–Malavasi–Menziani–Cormack–Segre) one, has been extended to multicomponent borate and borosilicate glasses.

The success of the earliest PMMCS FF has been due to its simplicity, transferability, and good accuracy in the reproduction of the structure and properties of silicate and aluminosilicate glasses.[40–55] The BMP FF has been demonstrated to strongly improve its performances thanks to the inclusion of T–O–T three-body interactions coupled with T–T repulsive interactions (T = Si, P, Al) that allow a better reproduction of the T–O–T BAD, Q^n speciation, and density.

The results shown that the BMP FF enriched with reliable boron–oxygen (and consequently B–O–B, B–O–Si, B–B, and B–Si) parameters gives performance similarly and, in some cases, even better than polarizable FFs. Therefore, this extended FF will constitute a useful tool for the academic and industrial researchers to unravel composition–structure–properties relationships in multicomponent borate and borosilicate glasses and develop new glass formulations with tailored properties.

2 | METHODOLOGY

2.1 | The force-field functional form

The BMP FF is based on a rigid ionic model, with partial charges to handle the partial covalency of the Si–O bond in silicate systems. It is given by the combination of two-body terms (Equation 1) describing the T–O, (T = Si, Al, P, B) and O–O interactions through a long-range Coulomb potential, a short-range Morse function, and a repulsive contribution of the form B/r^{12}, necessary to prevent atomic collapse at high temperature and pressure, with a three-body screened harmonic function (Equation 2) between T–O–T bridges (T = Si, P, B), and with a Buckingham repulsive interaction (Equation 3) between former elements that is needed to better predict the density of the glasses:

$$U\left(r_{ij}\right) = \frac{z_i z_j e^2}{r_{ij}} + D_{ij}\left[\left(1 - e^{-a_{ij}\left(r_{ij}-r_{ij}^0\right)}\right)^2 - 1\right] + \frac{B_{ij}}{r_{ij}^{12}} \tag{1}$$

$$U\left(\theta_{ijk}\right) = \frac{k_{ijk}}{2}\left(\theta_{ijk} - \theta_{ijk,0}\right)^2 e^{-\left(\frac{r_{ij}}{\rho} + \frac{r_{jk}}{\rho}\right)} \tag{2}$$

$$U\left(r_{ij}\right) = A_{ij}\, e^{\frac{-r_{ij}}{\rho_{ij}}} \tag{3}$$

The charges $z_{i,j}$ are fixed and consistent with the value of −1.2e for oxygen (thus $z_{Na} = 1.2$, $z_B = 1.8$, etc). D_{ij}, a_{ij}, and r_{ij}^0 are fitting parameters connected, respectively, to

TABLE 1 Compositions of the simulated glasses

Name	Composition	
NB*R*	$R(Na_2O) \cdot B_2O_3$	*R* = 0*, 0.05*, 0.11*, 0.18, 0.25*, 0.33, 0.43*, 0.67*, 1.86*, and 2.33*
LB*R*	$R(Li_2O) \cdot B_2O_3$	*R* = 0.11, 0.18, 0.25, 0.43, 0.54, and 0.67
MB*R*	$R(MgO) \cdot B_2O_3$	*R* = 0.30, 0.41, 0.61, 0.79, 0.82, 0.89, 1.00, 1.08, and 1.22
CB*R*	$R(CaO) \cdot B_2O_3$	*R* = 0.25, 0.33, 0.35, 0.43, 0.50, 0.56, 0.67, 0.72, 0.82, 0.89, 1.00, and 1.22
NB*RSK*	$R(Na_2O) \cdot K(SiO_2) \cdot B_2O_3$	*K* = 0.50 *R* = 0.10*, 0.20*, 0.33, 0.50*, 0.60*, 0.70, 0.80*, 0.90*, 1.00* *K* = 1.00 *R* = 0.20*, 0.33*, 0.40, 0.50*, 0.60*, 0.70, 0.90*, 1.00*, 1.20*, 1.30*, 1.60, 2.00*, 2.50*, 3.00, 3.50* *K* = 1.01 *R* = 0.68 *K* = 2.00 *R* = 0.10, 0.20*, 0.30, 0.40, 0.45, 0.50*, 0.55, 0.60, 0.65, 0.70*, 0.90*, 1.00*, 1.10, 1.20, 1.30, 1.50*, 2.00, 2.50*, 3.00, 4.00* *K* = 3.00 *R* = 0.80*, 1.00*, 1.50, 2.00*, 2.50, 3.00*, 4.00*, 5.00* *K* = 3.07 R = 1.36 *K* = 3.75 R = 0.79 *K* = 4.00 *R* = 1.00*, 1.50*, 2.00, 2.50*, 3.00*, 4.00*, 5.00, 6.00, 7.00* *K* = 4.46 R = 2.23* *K* = 4.52 R = 0.90* *K* = 5 *R* = 1.31*, 4.00* *K* = 6.00 *R* = 1.50*, 2.00, 2.50*, 3.00*, 4.00*, 5.00, 6.00*, 7.00*

Note: The asterisk symbol denotes glass compositions used to fit the *D*(*R*,*K*) model presented in Section 2.3.4.

the dissociation energy, curvature ($2Da^2$), and reference minimum position of the Morse function.

2.2 | Glass generation through classical molecular dynamics simulations

Sodium, lithium, calcium, and magnesium borate and sodium borosilicate glasses with compositions reported in Table 1 and named NB*R*, LB*R*, CB*R*, MB*R*, and NB*RSK*, where $R = ([A_2O]+[AEO])/[B_2O_3]$ (A = Na and Li, AE = Ca and Mg) and $K = [SiO_2]/[B_2O_3]$, from hereafter, respectively, were generated through classical MD simulations by using the melt-quench approach.[52] NB0 refers to pure B_2O_3.

The fitting procedures of the final *D*(*R*,*K*) model presented in Section 2.3.4 were performed on the NB*R* and NB*RSK* glasses (59 out of 114) marked with an asterisk in Table 1, using boxes containing ~400 and ~1500 atoms as it will be detailed later, whereas the other glasses were used for validation of the final model. In the latter case, two series of structural models were generated for the simulation and analysis of different properties. The first series consisted of boxes containing ~1500 atoms and was used to investigate short- and medium-range order. The second series consists of small boxes containing ~400 atoms and was used to compute ^{11}B, ^{17}O, and ^{29}Si NMR parameters and simulate solid-state MAS NMR spectra. Three independent replicas for each composition were generated to improve the statistics of structural and MAS–NMR data. Glass composition and models are reported in Tables S1–S3. The leap-frog algorithm encoded in the DL_POLY package[56] was used to integrate the equation of motion with a time step of 2 fs. The initial configurations were generated by placing randomly the number of atoms in a cubic box, the dimension of which allows the experimental density to be reproduced.

The simulations performed during the fitting procedure were made in the NVT ensemble, equilibrating the system at 2000 K for 20 ps ensuring a suitable melt of the samples, then cooling to 300 K at a nominal cooling rate of 5 K/ps and equilibrating at 300 K for 200 ps. As the quench rate is known to affect the N_4 fraction and NBO speciation in borosilicate glasses,[57] some tests were performed using rates of 1 and 0.5 K/ps. Although the amount of the N_4 species slightly increases by decreasing the quench rate, the differences are smaller than the deviation obtained

on three replicates. For these reasons, we decided to use 5 K/ps, in order to decrease the computational cost. The pressure, during the NVT quenching, ranged from 1.0 to −2.0 katm.

The simulations made for the structural analysis and properties calculations of all the tested compositions were performed in the NPT ensemble, after a short NVT optimization at high temperature, at a constant pressure of 1 bar using the Berendsen barostat[58] with frictional constants set to 0.2 ps, and following the procedure described earlier.

Coulomb interactions were calculated by the Ewald summation[59] method with a cutoff of 12 Å (1500 atoms boxes) and 8 Å (400 atoms boxes), whereas short-range cutoff values of 7 Å for the Van der Waals interactions.

2.3 | Fitting strategy

The empirical fitting used followed the protocol described as follows:

(i) Relaxed fitting on crystal structures
(ii) Design of experiment
(iii) Bayesian optimization
(iv) Creation of a model for the D parameter dependent on the R and K ratios.

2.3.1 | Relaxed fitting on crystal structures

First, as in the original derivation, the B–O, B–B, and B–Si pair potentials and the B–O–B and B–O–Si three-body interaction were obtained by using the relaxed fitting[60] procedure encoded in the GULP[61] code using the experimental crystalline structure[62–69] of B_2O_3, $LiBO_2$, LiB_3O_5, $Na_3B_3O_6$, $Mg_2B_2O_5$, $Ca_3B_2O_6$, $NaBSiO_4$, and $NaBSi_3O_8$.[62–69] In this way, a first guess of the parameters was obtained. Only the θ_{ijk} value of the three-body interaction was kept fixed at 109.47° as it is for all the triplets already parameterized.[36] The choice of the reference angle was biased by the sp^3 hybridization of BO atoms, derived from the valence bond theory.[70,71] According to this theory, BO atoms have four surrounding electron pairs, two of which are bonding pairs and two are lone pairs, ideally oriented along the vertices of a tetrahedron with angles of 109.47°. The deviations from this angle are due to repulsion between the orbitals and elements bound to the central atom. Obviously, this is a large simplification of the combination of classical and quantum effects governing the geometry of these systems. We emphasize that different choices could be made for the reference angle. For example, it can be considered a fitting parameter, as in the popular ReaxFF,[72] or fixed at experimental value, but the physical meanings would be questionable, as in borate and borosilicate glasses, the (B, Si)–O–(B, Si) angles cover a broad range of values.

Any fitting procedure aims to minimize a cost function that quantifies the distance of the results obtained with a set of parameters with the target ones. In this work, we used the sum of squares function F defined as follows:

$$F = \sum_{i=1}^{M} w_i \left(f_{i,obs} - f_{i,MM} \right)^2 \quad (4)$$

where M is the total number of observables used during fitting, w_i is a weighting factor for each observable, and $f_{i,obs}$ and $f_{i,MM}$ are the target (experimental or QM-computed) and the MM-computed observables, respectively.

In the relaxed fitting method, $f_{i,MM}$ are the observables (structure and properties) computed after a geometry optimization. This means that the structure is optimized at every step in the fit, and the displacements of the structural parameters are calculated instead of the energy gradients as used in conventional fitting. It is worth noting that this is a minimization process in the space of the force-field parameters, and thus the minimization algorithm (BFGS in this work) stops when the closest relative minimum is reached.

To better sample the parameter space, we used different initial parameters D, a, r^0, and k. The initial B–O, B–O–Si, and B–O–B parameters ranged between $0.8 \leq D \leq 2.8$, $2.0 \leq a \leq 3.5$, $1.4 \leq r^0 \leq 1.6$, and $10 \leq k \leq 100$, whereas the starting A and ρ parameters of the repulsive B–B and B–Si Buckingham interaction were set to the analogs Si–Si parameters of the BMP potential.[36] From this fitting, an initial set of parameters was obtained for further refinement (D = 1.06223 eV, a = 2.60414 $Å^{-2}$, r^0= 1.543656 Å, k_{B-O-B} = 60 eV/rad^2, k_{B-O-Si} = 60 eV/rad^2, A_{B-B} = 8.9594 eV and ρ_{B-B} = 0.8012 $Å^{-1}$, A_{B-Si} = 8.9594 eV and ρ_{B-Si} = 0.9270 $Å^{-1}$). These parameters were tested on the sodium borate (NBR) series but give poor results on the BO_3/BO_4 speciation (see Figure 2) because of the very complex boron chemistry in glasses that cannot be fully parameterized using only crystalline structures. For this reason, we decided to study the effects of the potential's parameters by the means of the design of experiment approach applied directly on glasses, as described in the following section.

2.3.2 | Design of experiment to study the effects of the parameters

The effect of the Morse (D, a, and r^0) and three-body interaction (k) parameters, and their combination on the responses, was studied exploiting a "screening" full

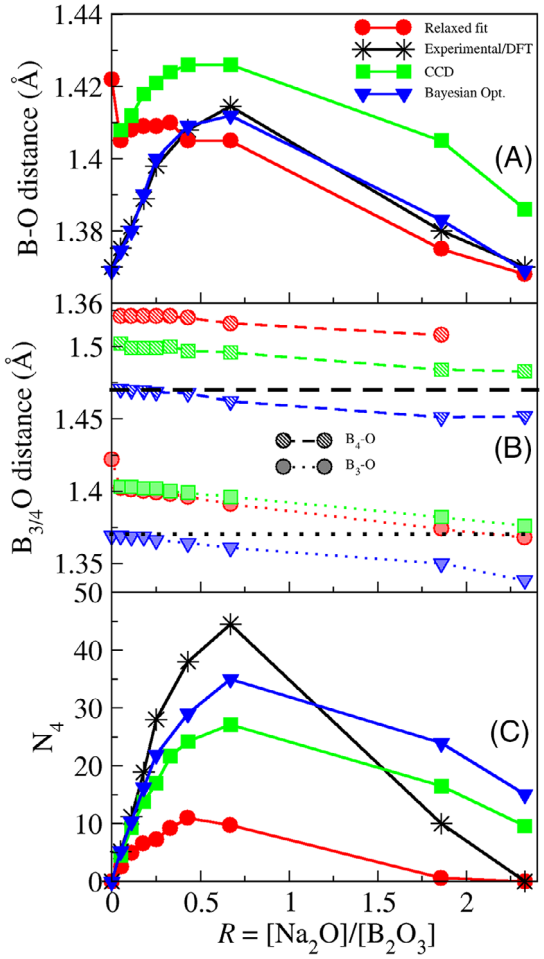

FIGURE 2 Comparison among average B–O (panel a), B_3–O, and B_4–O (panel b) distances calculated with the force-field parameters fitted on crystals, obtained from the central composite design (CCD), and Bayesian optimization. Comparison between experimental[15] and simulated N_4 species (panel c)

factorial design (FFD)[73] and a subsequent "modeling" central composite design (CCD),[74–76] from which a set of parameters was derived. Details about the two designs of experiment are reported in dedicated Section S2.

The considered responses were the N_4 fraction and the B–O distance in NB0.25, NB0.67, and NB1.86 glasses. The choice of these compositions was made to encompass different parts of the N_4 versus R curve without considering the NBS glasses to simplify the model. In particular, one glass (NB0.25) in the first region, where N_4 increases, one at the top of the curve (NB0.67), and one in the last region (NB1.86), where N_4 decreases, were chosen. Experimental values[15] of the N_4 fraction are 28.0%, 44.5%, and 9.7% for NB0.25, NB0.67, and NB1.86, respectively. The value of the target B–O distance was calculated by considering the B^3–O distance as 1.37 Å and B^4–O distance as 1.47 Å (values predicted by density-functional theory [DFT] calculations),[1,66] and applying a weighted average based on the experimental BO_3 and BO_4 fractions. The values obtained are 1.398, 1.429, and 1.380 Å for NB0.25, NB0.67, and NB1.86, respectively.

The simulation boxes used here contained 400 atoms to limit the computational cost. As reported in Section S2, each point of the DoE was replicated once, except for the central point, for which three replicas were performed to evaluate the statistical deviation. The final set of parameters was tested on three independent simulations of systems containing 1500 atoms.

The FFD revealed that only the three Morse parameters have a significant effect on the responses, whereas the effect of the three-body interaction's constant is negligible. The central point of the FFD ($D = 1.45$, $a = 2.9$, and $r^0 = 1.5$) was also used to define the central point of the CCD, where only Morse's parameters were considered. The three-body constants and the B–B and B–Si repulsive interactions were fixed at the values found from relaxed-fitting on crystals. As for the latter two interactions, we realized that their main impact is on the glass density, with only minor effects on the other properties. For this reason, we decided to keep them fixed, allowing us to reduce the dimensionality of the parameters' space and the computational cost of the fitting procedure. The CCD allows the investigation of the quadratic effects and produced an optimal set of parameters ($D = 1.5624$, $a = 2.95$, and $r^0 = 1.4889$) in the factor space considered. These optimal parameters were used to simulate the sodium borate series; the variation of N_4 fraction with R is reported in Figure 2. The set of parameters obtained from CCD underestimates the increasing part of the N_4 curve ($R < 0.5$) and overestimates the decreasing part ($R > 0.5$). The mean absolute error (MAE) on N_4 for the full glass series is 8.4. This is acceptable by considering the fixed-parameter nature of the potential but much larger than that obtained using Du and Stevensson–Edén potentials (see Section 3). The B–O distances are systematically overestimated by 0.03–0.04 Å.

For this reason, we attempted to optimize the parameters using the Bayesian optimization approach described in the following section.

2.3.3 | Bayesian optimization

Bayesian optimization[77,78] is a machine learning–based approach to optimize black-box objective functions that take a long time to evaluate and for which derivatives are not available. It is best suited for optimization over continuous domains of less than 20 dimensions and tolerates stochastic noise in function evaluations.

After evaluating the objective function according to an initial space-filling experimental design, often choosing points uniformly at random within a defined domain,

a surrogate function is built for the objective and the uncertainty in that surrogate is quantified using Gaussian process regression.[79] Then an acquisition function defined from this surrogate is used to decide where to sample the next point. At this point, the real objective function is then evaluated, and the surrogate function is updated. The process is repeated iteratively for a number of times decided by the user.

In this work, a homemade Python script exploiting the bayes_opt package[80] has been used to explore a domain of parameters $D = [1.5–2.7]$, $a = [2.5–3.0]$, and $r^0 = [1.40–1.50]$. The upper confidence bound (UCB) acquisition function was employed,[81,82] which minimizes the regret throughout the optimization. The form of the acquisition function is

$$\begin{aligned} a_{\mathrm{UCB}} &= (x;\{x_n, y_n\},\theta) \\ &= \mu(x;\{x_n, y_n\},\theta) - k\sigma(x;\{x_n, y_n\},\theta) \end{aligned} \quad (5)$$

where $\{x_n : y_n\}_{n=1}^{N}$ are the observables, θ is the step (number of observations), μ indicates the predictive mean function, σ is the predictive standard deviation function, and k is a tunable parameter that balances exploitation and exploration. In this work, the default value (2.576) has been used.

As for the constant of the three-body terms and parameters of the repulsive interactions, we kept the values fitted previously on crystals, which reproduce the B–O–B and B–O–Si angles in crystals with a MAE of 3.8° and 1.9°.

We first tried to optimize the B–O parameters using the same three sodium borate glasses used for the DoEs: NB0.25, NB0.67, and NB1.86, respectively. As it was done for the DoEs, we used 400 atoms systems as we expected a large number of optimization steps (for each step, the simulation of three glass models had to be performed). Every time a set of parameters seemed promising, it was tested on simulation boxes containing 1500 atoms performing three replicas.

As objective (cost) function to minimize, we used the sum of squares function (Equation 4) using as observables the experimental N_4 fraction and the B–O distance of these three glasses simultaneously (see the previous section). To ensure that each observable has the same impact (in terms of order of magnitude) on the cost function, we used weights of 1 and 10 000 for the N_4 fraction and B–O distances, respectively, as the deviation of the B–O distance is the order of 10^{-2} (10^{-4} when squared), whereas for N_4, it is on the units.

After 200 iterations, the best parameters found were: $D = 2.337$, $a = 2.643$, and $r^0 = 1.43667$. The trends for the N_4, average B–O, and $B_{3/4}$–O distances with R obtained with this set of parameters are also reported in Figure 2.

The MAEs on the N_4 and average B–O distances are 6.9 and 0.002, respectively. Panel (b) of Figure 2 shows that the set of parameters obtained from the Bayesian optimization can reliably reproduce the B_3–O and B_4–O distances obtained from DFT calculations,[83,84] displayed with dotted and dashed black lines, showing a decreasing trend. This is expected as the number of B–NBO bonds increases with R and B–NBO bond distances are expected to be shorter than B–BO ones. Albeit the Bayesian optimized set of parameters predicts excellently the B–O distance, the N_4 curve is still not reproduced with the desired accuracy. For this reason, we decided to make the $D_{\mathrm{B–O}}$ parameter dependent on the glass composition (R- and K-ratios) as described in the following section.

2.3.4 | Creation of a model for the D parameter dependency on the R and K ratios

As observed in the previous section, neither set of composition-independent parameters provides satisfactory results in the calculation of the N_4 fraction. As the set of parameters obtained from the Bayesian optimization provides excellent B–O distances, we decided to start from these parameters and to make the $D_{\mathrm{B–O}}$ parameter of the Morse function dependent on R and K while maintaining fixed the a_{ij} and r^0 parameters to 2.643 and 1.43667, respectively.

First, optimal values of the $D_{\mathrm{B–O}}$ parameters that allow reproducing the N_4 fraction for the glasses of the NB and NBS series (marked with an asterisk in Table 1) with high accuracy have been determined by using the Bayesian optimization approach. In this case, we used 1500 atoms systems as the optimization was made on one glass at a time and on only one parameter, so the reduced number of simulations expected allowed reducing the computational times. On average, 30 steps were needed to obtain each optimal D values reported in Figure 5 (blue dots).

Subsequently, we fitted the model shown in the following equation:

$$\begin{aligned} D_{\mathrm{model}} &= a(R)\cdot e^{b(R,K)} + c(R)\cdot e^{d(R,K)} + 0.001665\cdot K^3 \\ &\quad - 0.12807\cdot R \\ a(R) &= 2.11081 + \frac{1}{(R+1)^2} \\ b(R,K) &= 0.02063\cdot R + 0.06312\cdot K \\ c(R) &= -2.12213 + \frac{1}{(R+1)^2} \\ d(R,K) &= -7.50152\cdot R + 0.32778\cdot K \end{aligned} \quad (6)$$

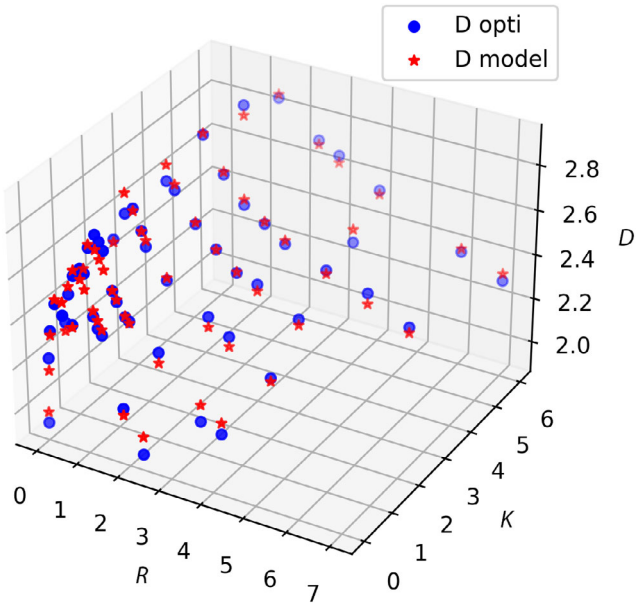

FIGURE 3 Fitting model: comparison between optimal and modeled D_{B-O} values for the different borate and borosilicate glasses

The choice of the previous equation was derived from mathematical intuition after observing the trends of the optimal D values as a function of R and K. To describe the ascending and descending trends, two exponential functions with prefactors and arguments dependent on R and K was necessary. Simple functions of R and K were tested, and after a few attempts, the functions $a(R)$, $b(R,K)$, $c(R)$, and $d(R,K)$ were found to be optimal to reproduce the whole trend.

Figure 3 shows the fitting of the D values for the NB ($K = 0$) and NBS glasses where the modeled D_{B-O} values are reported as a function of R and K following Equation (6).

The MAE of the D_{B-O} calculated with the fitted model with respect to the optimal one is 0.0314 eV and of the N_4, calculated for the full NB and NBS glass series, results in 2.7 units, as detailed in Section 3, confirming the huge improvement of the prediction ability of this new variable set of parameters.

The final parameter for B–O, B–B, B–Si, B–O–B, and B–O–Si interactions are shown in Table 2, the other parameters of the BMP force-field can be found in Table S9. As for the other potentials tested in this work, we refer to the original papers. The overall flowchart of the parameterization process is reported in Figure 4.

2.4 | Re-parametrization of Mg–O interaction

Since during the employment of the new B–O parameters in the simulation of the Mg-containing borate glasses, we realized that the original Mg–O parameters did not perform with the desired accuracy we decided to refit them. This was done by exploiting the Bayesian optimization method to minimize the difference between the experimental and simulated N_4 fraction, density, Mg coordination, and the Mg–O distance of the MB1.00 glass. The obtained parameters have been tested on the simulation of the experimental structures of silicate[85,86] ($MgSiO_3$, $Mg_2Si_2O_6$) and borate[87] ($Mg_2B_2O_5$) crystals using the optimization method implemented in the GULP code, giving a MAE on the Mg–O distance of 0.14 Å, which corresponds to the 6.9% of error. The new parameters are listed in Table 2, whereas the results will be shown in the following sections.

TABLE 2 Parameters developed in this work for all the boron and magnesium interaction present in the BMP force field

Morse	D_{ij} (eV)	a_{ij} (Å^{-2})	$r^0{}_{ij}$ (Å)	B_{ij} (r^{12})
B$^{1.8}$–O$^{-1.2}$	Equation (5)	2.643330	1.436670	10.0
Mg$^{1.2}$–O$^{-1.2}$	0.010000	2.554310	2.610518	5.0
Screened harmonic	K_{ijk} (eV rad^{-2})	$\theta^0{}_{ijk}$ (°)		
B–O–B	60.0	109.47		
B–O–Si	60.0	109.47		
Buckingham	A_{ij} (eV)	ρ_{ij} (Å^{-2})		
B–B	8.9594	0.8012		
B–Si	8.9594	0.9270		

3 | RESULTS AND DISCUSSION

In this section, the results of the computational simulations on sodium, lithium, magnesium, and calcium borate and sodium borosilicate glasses are reported and compared with the available experimental data. A comparison with the Bauchy, SHIK, Du, and Stevensson–Edèn potentials is also reported using data extracted directly from the literature,[26–30,35] or computing them following the computational procedures described in the original papers.

3.1 | N_4 fraction

The boron speciation is a very important structural feature that affects the macroscopic properties of the glass,[88–90] such as thermal and mechanical properties. As already discussed in the introduction, the N_4 fraction varies in a nonlinear way with the composition, and the prediction of the correct speciation is a very important challenge for classical FF.

Figure 5 shows the N_4 fraction in the four studied borate series with different modifier elements, calculated using

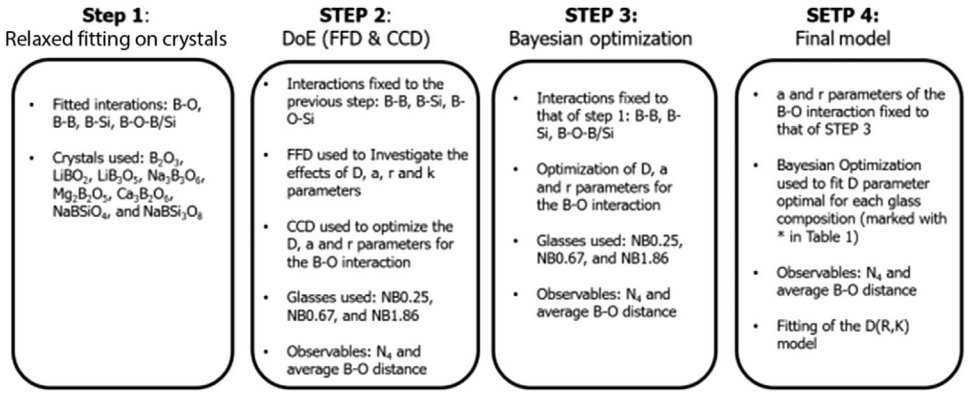

FIGURE 4 Flowchart of the force-field development procedure adopted

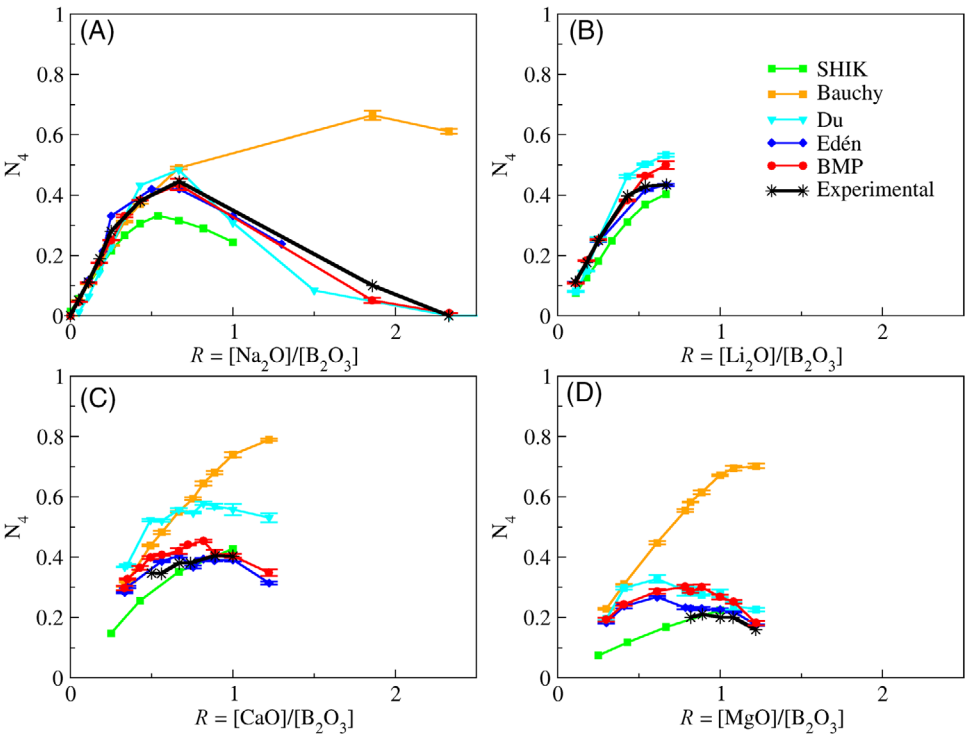

FIGURE 5 Comparison of the N_4 fraction obtained with BMP, Du, Bauchy, SHIK, and Stevensson–Edén potentials and experiment[89,91–94] for sodium (A), lithium (B), calcium (C), and magnesium (D) borate glasses

different potentials and compared with experimental data.[89,91–94] The new BMP parameterization proposed in this work satisfactorily predicts this property for all the studied compositions (notwithstanding the fitting was made only on sodium borates and borosilicates) giving the best agreement with experimental data for all the alkali borate compositions and a good agreement for alkaline-earth ones. As for the MB series, even with the new Mg–O parameterization, the N_4 fraction is overestimated for glasses with R values <1. However, the new parameters are the best compromise reachable with the simple functional form employed to reproduce fairly well not only the N_4 fraction, but also the Mg–O distance, Mg coordination, and the density of the glasses. During the optimization, we observed that to have a lower N_4 fraction, the Mg–O distance had to be unrealistically very short (~1.7 Å). For these reasons, we preferred to have higher N_4 in some compositional regions but physically meaningful Mg data.

Figure 6 shows a comparison of the experimental[15,20] and simulated N_4 fraction in borosilicate glasses. Furthermore, a comparison with the Du FF (which has variable parameters depending on the composition

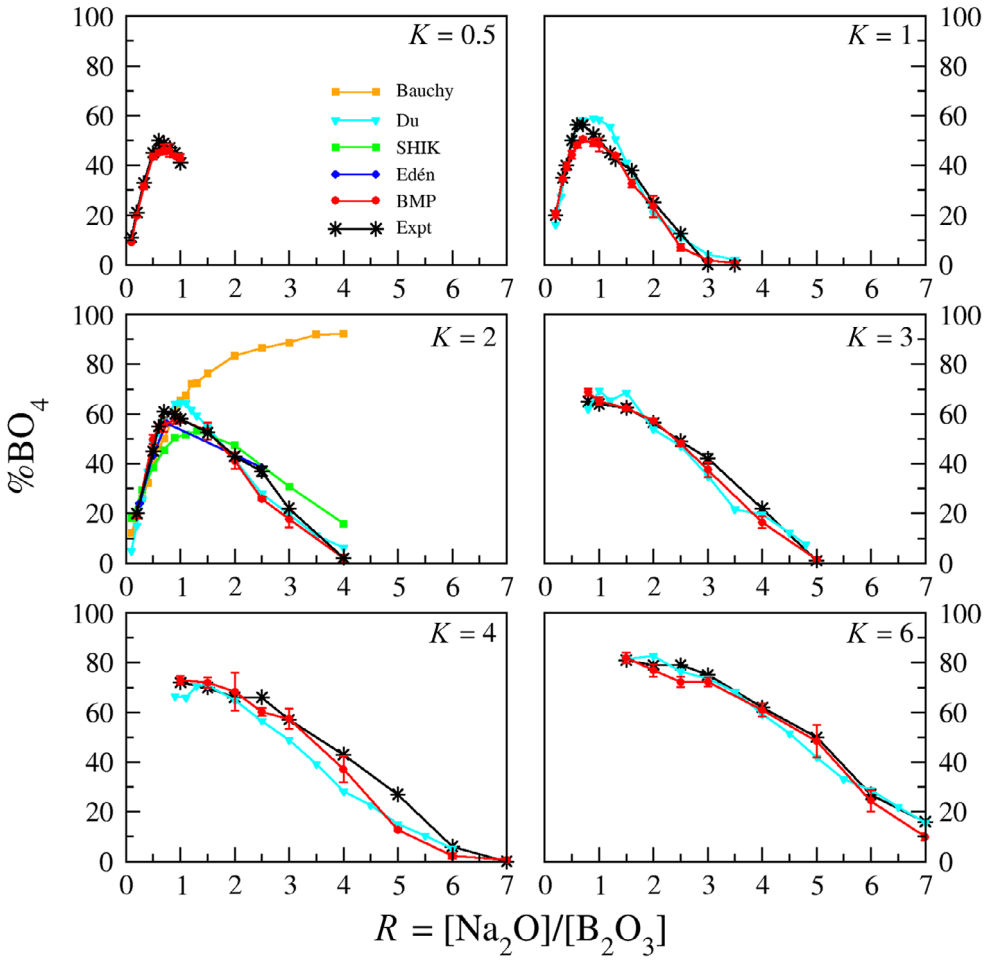

FIGURE 6 Comparison of the experimental[15,20] and simulated N_4 fraction in sodium borosilicate glasses with different K values

and on the expected N_4) is reported for glasses with $K \geq 1$,[27] and with SHIK, Bauchy, and Stevensson–Edén FFs[26,28,30,34] for $K = 2$.

The BMP potential accurately reproduces the N_4 fraction in the whole compositional range succeeding in reproducing the nonlinear trends at the different K values thanks to the variable D_{B-O} parameter. An MAE of 2.7% on the N_4 fraction was observed. The Bauchy potentials predict good N_4 data for the borate and borosilicate series investigated only at R-values lower than R_{max}. Stevensson–Edén's potential, which relies on the more sophisticated core-shell model, can excellently predict the N_4 fraction for all the compositions, but this comes at the price of a more time-consuming procedure (the core-shell model needs shorter time steps to take into account the shell vibrations). The Du potential gives good agreement with experiments on alkali borate and borosilicate glasses, whereas a strong overestimation is visible for alkaline-earth borates, and especially for calcium borates. SHIK potential reproduces well the trend for the N_4 fraction in alkaline borate and borosilicate series, but it tends to slightly underestimate it for compositions with R close to R_{max}.

3.2 | Density

Figure 7 shows the comparison between the experimental[95–100] and predicted densities calculated with the tested FFs for the studied borate and borosilicate glasses. For the sake of clarity, only the NBS series with $K = 2$ is reported. Densities of all the NBS glasses can be found in Figure S3.

BMP potential reliably reproduces the density values and the positive trends for all the studied compositions. In particular, density is overestimated for sodium borates at high R-values (max error = 0.18 g/cm^3, so the 7.8%, when $R = 0.67$). In addition, a slight overestimation in LB series and underestimation in CB series are present (max error = 0.07 and 0.13 g/cm^3, so 3.1, and 4.7%, respectively). As for the MB series, the new boron and magnesium parameters give very satisfactory results on density data.

All the studied potentials reproduce fairly well the increasing trend of the density when more modifiers are added to the composition and the plateau that this property reaches at high Na_2O content.

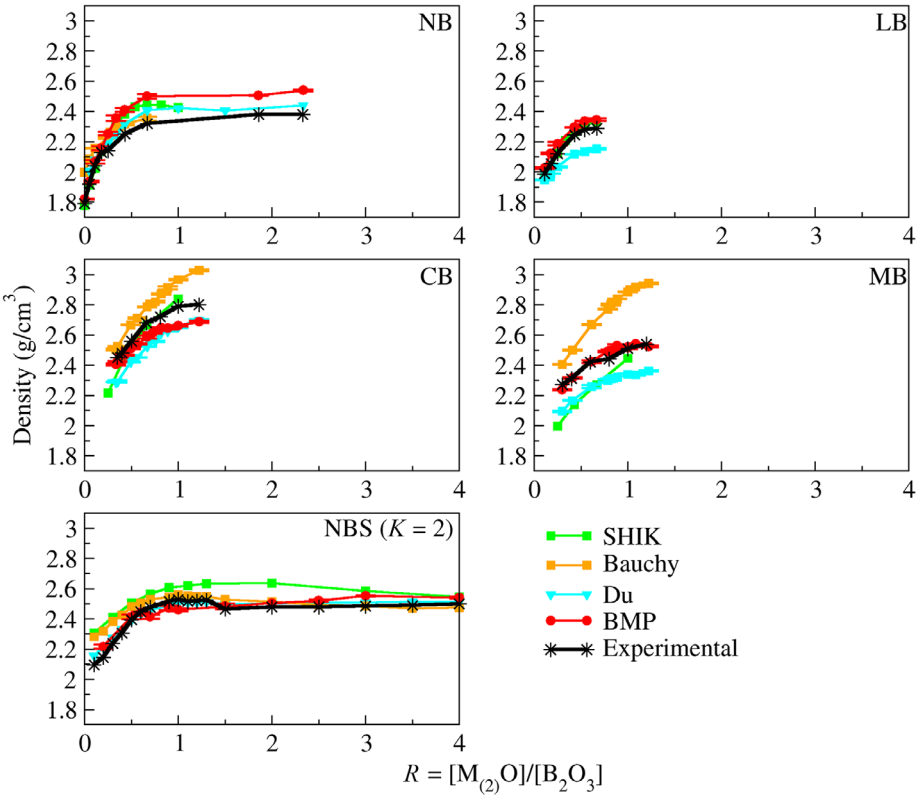

FIGURE 7 Comparison of the density obtained with BMP, Du, Bauchy, and SHIK potentials and experiment[95–100] for sodium, lithium, calcium, and magnesium borates and sodium borosilicate with $K = 2$

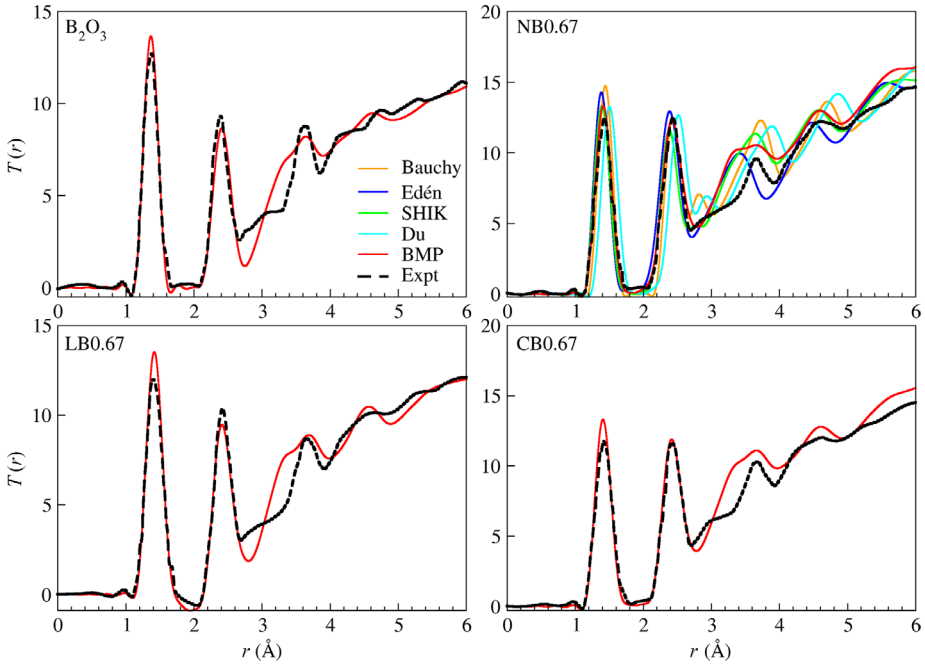

FIGURE 8 Comparison between experimental[101,102] and simulated neutron total distribution function ($T(r)$) of B_2O_3, NB0.67, LB0.67, and CB0.67 glasses. For the NB0.67, a comparison with other force fields (FFs) performance is shown.

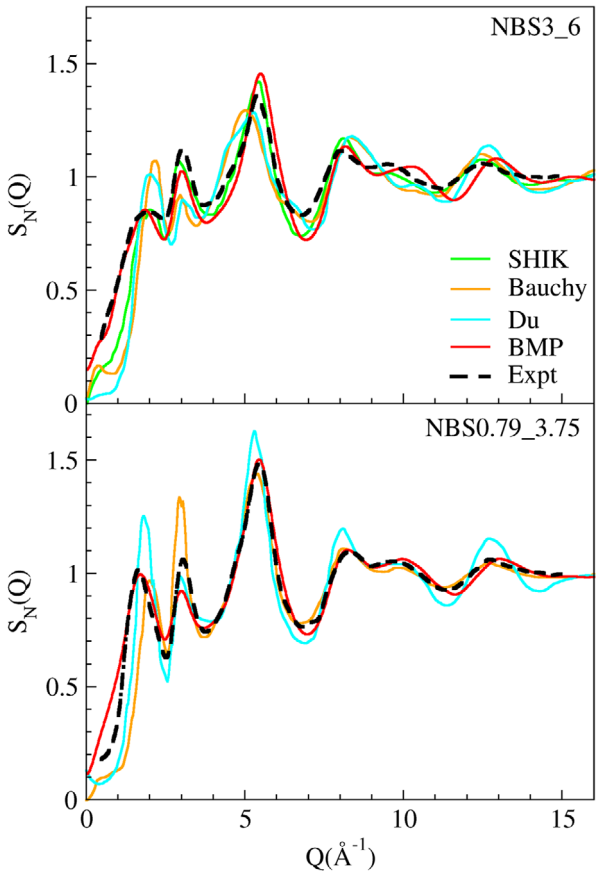

FIGURE 9 Comparison between experimental[24] and simulated neutron structure factors for NBS3_6 and NBS0.79_3.75 glasses

The Bauchy potential gives very good results on sodium borate and borosilicate glasses, even if it tends to overestimate the density for all the studied series. The SHIK FF gives good agreement for LB and CB series, whereas it underestimates the density of the MB series and systematically overestimates it in NB and NBS series. Du's potential gives a very good estimation of the increasing trend of the densities along with the glass series, but it gives a systematic underestimation of the LB, CB, and MB series. The Stevensson–Edén potential has not been tested on this property because we have realized in a previous investigation that the density is not a reproduce well with the actual parameterizations of core-shell potential.[36] As for the NBS glasses, the BMP reliably reproduce the trend of the density with increasing R values, leading to an MAE of 0.06 g/cm^3 on the complete NBS series.

3.3 | Neutron diffraction spectra

Figure 8 reports the experimental[101, 102] and simulated spectra of B_2O_3, NB0.67, LB0.67, and CB0.67 glasses. The formula and methods used to simulate the neutron diffraction total distribution functions are reported in the Supporting Information of our previous work[36] as well as in Refs. [104, 105].

A good agreement with the experimental total distribution functions ($T(r)$) is observed, especially regarding the position and shape of the first two peaks at 1.4 and 2.4 Å, which are related to the B–O and B–B and O–O distances, respectively.

Neutron diffraction spectra cannot distinguish the B^3–O and B^4–O different distances, but the correct computation of both of them, with the N_4 fraction, is fundamental to predict the spectra. The new parameterization proposed in this work predicts an average B^3–O distance of 1.368–1.377 Å and B^4–O of 1.465–1.476 Å, which are in very good agreement with the available experimental data.[1,83,84]

The section of the spectra from ~3 to ~5 Å is related to the medium-range order, and especially to the presence of ring structures. In particular, boroxol rings are massively present in B_2O_3 glass, where 60%–80% of boron atoms are in these rings and their amount decreases when the modifier content increases in the composition.[103] The third peak at ~3.6 Å is related to an intra-ring B–O distance between atoms not directly bonded.[17] This peak is higher in B_2O_3 glass, because of the higher amount of boroxol rings in its structure, whereas for the other glasses, it is lower. The BMP potential cannot predict accurately the shape of the peak, but it produces a larger band that encompasses the experimental peak. To our knowledge, there is no classical force-field that can predict accurately the ring structure of borate glasses. Among the tested potentials, the Stevensson–Edén and BMP FFs provide almost 5% and 4% of boron atoms in the boroxol rings for B_2O_3, respectively, whereas the other potentials do not produce any boroxol rings.

As for the comparison with other published FFs, BMP and SHIK potentials give the best agreement of the first two peaks and do not predict a third, small, peak at ~2.8–3.0 Å as Du and Bauchy potentials do. This third peak, which is not present in experimental data, is given by different predicted B–B distances. The complete deconvolution of the total distribution function given by the atomic distances is reported in Figure S6.

To quantify the agreement between the computed total correlation function $T^{calc}(r)$ with the diffraction data $T^{exp}(r)$, the former has been broadened to account for the limit of the momentum transfer (Q_{max}) in diffraction experiments,[86] and the R_x factor proposed by Wright[104,105] has been computed:

$$R_x = \sqrt{\frac{\sum_{i=1}^{N}\left[T^{\mathbf{exp}}(R_i) - T^{\mathbf{calc}}(R_i)\right]^2}{\sum_{i=1}^{N}\left[T^{\mathbf{exp}}(R_i)\right]^2}} \cdot 100 \qquad (7)$$

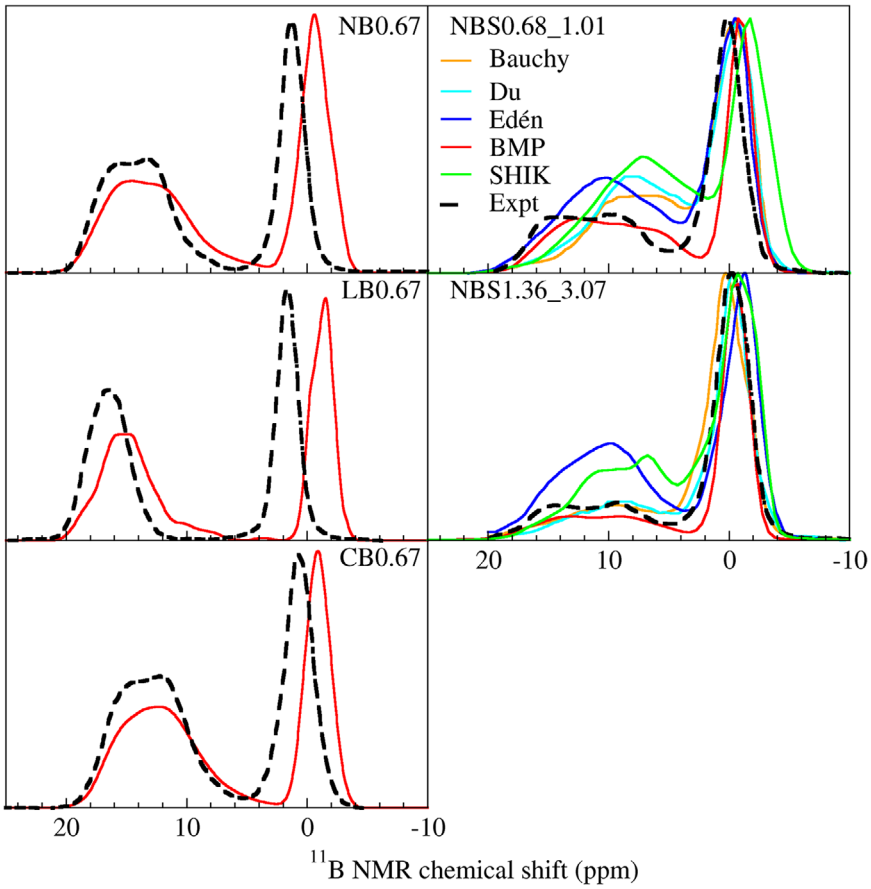

FIGURE 10 Simulated and experimental[23,106,107] ^{11}B magic angle spinning (MAS) nuclear magnetic resonance (NMR) spectra of NB0.67, LB0.67, CB0.67 (14.1T), NBS0.68_1.01, and NBS1.36_3.07 (11.7T) glasses

The R_x values calculated from the data obtained with the different tested potentials on NB0.67 glass are 13.75, 22.05, 13.60, 14.70, and 13.38 using Bauchy, Du, SHIK, Edén, and BMP potential, respectively.

The R_x values calculated using BMP potential for the other glasses shown in Figure 8 are 9.89, 10.73, and 20.27 for B_2O_3, CB0.67, and LB0.67, respectively.

As for the borosilicate glasses, a comparison between experimental[24] and simulated neutron structure factor $S_N(Q)$ of two glasses is reported in Figure 9.

The BMP potential shows excellent agreement with experimental data and overcomes the performances of Du and Bauchy's FFs,[34] especially in the first part of the spectra, which is relative to higher atomic distances in the medium-range order. Although the latter two potentials give the worst results, the SHIK[28] one performs similarly to the BMP and provides very good agreement with the experiment.

3.4 | NMR spectra

NMR is a very powerful experimental technique for the investigation of the short- and medium-range order of the glass structure. NMR signal depends on the local environment of the active nuclei. However, the disordered structure of glasses causes a broadening of the signal and the interpretation of experimental NMR spectra is often very difficult.[36] The details on the computation of the NMR parameters and spectra are reported in Section S8.

Figure 10 reports the comparison between experimental[92,106,107] and simulated ^{11}B MAS NMR spectra of one sodium, one lithium, and one calcium borate and two sodium borosilicate glasses. In all the ^{11}B spectra, the broadest peak, at higher chemical shift values, is relative to three-coordinated boron, whereas the four-coordinated one gives the thinnest peak, at lower chemical shifts. The shape of the simulated ^{11}B spectra is well reproduced by the BMP potential, showing the right separation between B^3 and B^4 signals. This is given by the appropriate simulation of the boron partition between BO_3 and BO_4 and can be ascribed to a good reproduction of the BADs (see Section S6) and B–O partial radial distribution function.[35]

The slight differences in the position of the B^3 peak (<1 ppm for NBS glasses, <2 ppm for NB0.67 and CB0.67, and <5 ppm for LB0.67) can be due to little differences in the B^3–O distances obtained with BMP potential when compared with the experiment. These differences are very small and could be resolved with DFT optimization

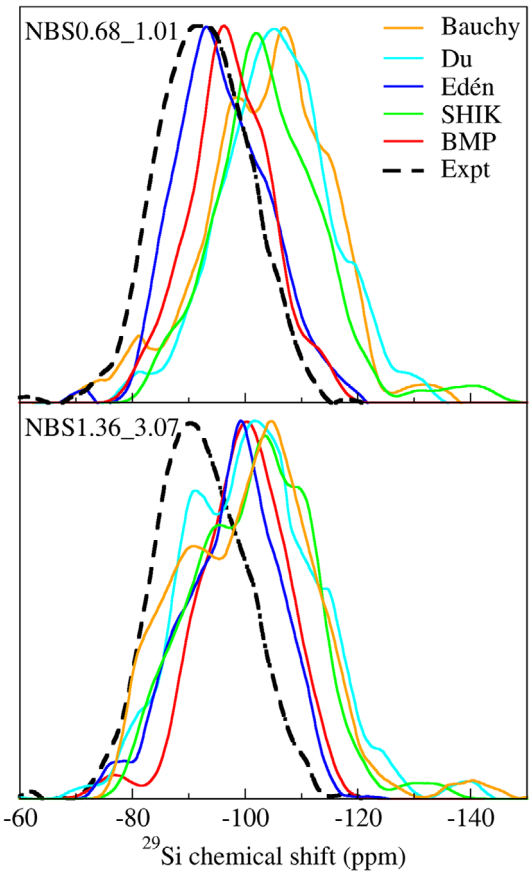

FIGURE 11 Simulated and experimental[35,29]Si magic angle spinning (MAS) nuclear magnetic resonance (NMR) spectra of NBS0.67_1.01 and NBS1.36_3.07 glasses obtained at 4.7T

of the structure, maintaining the shape of the spectra given by the MD simulation. The comparison with the other potentials[35] shows that the BMP is the only one that provides good shape and position of the B^3 and B^4 signals in NBS glasses. In particular, the separation between the two peaks and the shape of the B^3 one is well reproduced only by the BMP. Edén and SHIK potentials overestimate the B^3 peak, whereas Du and Bauchy do not show a good separation of the signals in NBS0.68_1.01 glass, and of the peak shape in the NBS1.36_3.07 glass.

Figure 11 reports the comparison between experimental[35] and simulated ^{29}Si MAS NMR spectra of two borosilicate glasses. The Stevensson–Edén potential provides the best accuracy in the reproduction of the shape and position of the signal, and the BMP FF almost reaches the same performance for NBS3_6 glass, whereas for NBS0.68_1.01, the peak is slightly shifted to lower chemical shifts. The differences between the BMP and Stevensson–Edén potential performances in the simulation of ^{29}Si NMR spectra probably originate from different predictions of Si[Q^n] and BADs. In fact, more connected Si species give lower chemical shift values.[108–111] Stevensson–Edén potential gives a network with 3.93 bridging oxygens per silicon in NBS0.68_1.01 glass, whereas BMP gives 3.82 BO/Si. This difference is less pronounced in the NBS1.36_3.07 glass, where the Edén and BMP potentials provide 3.73 and 3.69 BO/Si, respectively. Another cause of this shift is the different Si–O–B and Si–O–Si BAD. It is well known that smaller angles lead to higher chemical shifts,[35,36,112] and that thinner distributions tend to narrow the spectra. The Si–O–B BAD of NBS0.68_1.01 predicted with the Stevensson–Edén potential (see Figure S5) is centered at lower angles but is broader than the BMP's one. This is reflected in the ^{29}Si NMR spectra, which is broader and centered at higher chemical shifts.

Overall, among the considered rigid ion model potentials, the BMP provides the best agreement with experiments, both for the shape and position of the peaks, giving a well-resolved single peak, not provided by Bauchy and Du FFs, whereas the SHIK gives good shape only for NBS0.68_1.01 glass.

^{17}O MAS NMR spectra of NB0.67 glass has also been computed and compared with experiments[35] and are reported in Figure S7.

4 | CONCLUSIONS

In this paper, we have extended the BMP potential to borate and borosilicate glasses. A new model to derive the *D* parameter of the Morse B–O function as a function of the *R* and *K* ratios has been proposed and tested on four borate glass series with different modifier elements: sodium, lithium, calcium, and magnesium and on a sodium borosilicate glass series with compositions that cover a wide range of *R* and *K* values. The results obtained for structural characteristics, such as the N_4 fraction, density, %NBO, neutron TDF and $S_N(Q)$, ^{11}B, ^{29}Si, and ^{17}O NMR spectra of the aforementioned glass series can be summarize as follows: The BMP force-field gives satisfactory results for all the studied properties showing good agreement with experimental data. The limitation of the BMP highlighted in this paper is the difficulties in the reproduction of the medium-range order of borate glasses, especially at a low content of modifier. The latter is given essentially by the presence of super-structural units, such as boroxol rings. This feature is not reproduced by any of the tested potentials available in the literature, as highlighted by the comparison between the experimental and simulated neutron total distribution functions.

Obviously, the presence of the three-body interactions reduces the computational efficiency of the BMP potentials. Using the same system size and computational setting, the BMP potential takes nearly 3.5 times the SHIK and twice the Du and Bauchy computational time.

However, BMP potential is 10 times more efficient than the FFs based on the core-shell model, which needed much shorter time step required to decouple shell and core dynamics.

ACKNOWLEDGMENT

Annalisa Pallini thanks his past graduated student Luca Mascia for a preliminary work carried out during his graduation thesis in the corresponding author's group. The work was not granted by any funding agency or industry.

Open Access Funding provided by Universita degli Studi di Modena e Reggio Emilia within the CRUI-CARE Agreement.

ORCID

Marco Bertani https://orcid.org/0000-0002-0434-1238
Marina Cocchi https://orcid.org/0000-0001-8764-4981
Maria Cristina Menziani https://orcid.org/0000-0003-3428-5297
Alfonso Pedone https://orcid.org/0000-0003-3772-7222

REFERENCES

1. Kreidl NJ, Fréchette VD, Pye LD. Borate glasses: structure, properties, applications. Springer: New York (NY), 1978. ISBN: 9781468433579. https://doi.org/10.1007/978-1-4684-3357-9
2. Fu Q, Rahaman MN, Fu H, Liu X. Silicate, borosilicate, and borate bioactive glass scaffolds with controllable degradation rate for bone tissue engineering applications. I. preparation and in vitro degradation. J Biomed Mater Res A. 2010;95A(1):164–71. https://doi.org/10.1002/jbm.a.32824
3. Januchta K, Youngman RE, Goel A, Bauchy M, Logunov SL, Rzoska SJ, et al. Discovery of ultra-crack-resistant oxide glasses with adaptive networks. Chem Mater. 2017;29(14):5865–76. https://doi.org/10.1021/acs.chemmater.7b00921
4. Januchta K, Youngman RE, Goel A, Bauchy M, Rzoska SJ, Bockowski M, et al. Structural origin of high crack resistance in sodium aluminoborate glasses. J Non-Cryst Solids. 2017;460:54–65. https://doi.org/10.1016/j.jnoncrysol.2017.01.019
5. Lin Y, Brown RF, Jung SB, Day DE. Angiogenic effects of borate glass microfibers in a rodent model: use of bioactive borate-based glass microfibers for angiogenesis. J Biomed Mater Res A. 2014;102:4491–9. https://doi.org/10.1002/jbm.a.35120
6. Rahaman MN, Day DE, Sonny Bal B, Fu Q, Jung SB, Bonewald LF, et al. Bioactive glass in tissue engineering. Acta Biomater. 2011;7(6):2355–73. https://doi.org/10.1016/j.actbio.2011.03.016
7. Lepry WC, Nazhat SN. Highly bioactive sol-gel-derived borate glasses. Chem Mater. 2015;27(13):4821–31. https://doi.org/10.1021/acs.chemmater.5b01697
8. Erdogan C, Bengisu M, Erenturk SA. Chemical durability and structural analysis of PbO–B_2O_3 glasses and testing for simulated radioactive wastes. J Nucl Mater. 2014;445(1–3):154–64. https://doi.org/10.1016/j.jnucmat.2013.10.025
9. Kim M, Corkhill CL, Hyatt NC, Heo J. Development, characterization and dissolution behavior of calcium-aluminoborate glass wasteforms to immobilize rare-earth oxides. Sci Rep. 2018;8(1):5320. https://doi.org/10.1038/s41598-018-23665-z
10. Lodesani F, Tavanti F, Menziani MC, Maeda K, Takato Y, Urata S, et al. Exploring the crystallization path of lithium disilicate through metadynamics simulations. Phys Rev Mater. 2021;5(7):075602. https://doi.org/10.1103/PhysRevMaterials.5.075602
11. Angeli F, Villain O, Schuller S, Charpentier T, de Ligny D, Bressel L, et al. Effect of temperature and thermal history on borosilicate glass structure. Phys Rev B. 2012;85(5):054110. https://doi.org/10.1103/PhysRevB.85.054110
12. Hubert M, Faber AJ. On the structural role of boron in borosilicate glasses. Phys Chem Glasses: Eur J Glass Sci Technol Part B: Struct Role Boron Borosilicate Glass. 2014;55(3):136–58.
13. Konijnendijk WL, Stevels JM. The structure of borate glasses studied by Raman scattering. J Non-Cryst Solids. 1975;18(3):307–31. https://doi.org/10.1016/0022-3093(75)90137-4
14. Smedskjaer MM, Mauro JC, Youngman RE, Hogue CL, Potuzak M, Yue Y. Topological principles of borosilicate glass chemistry. J Phys Chem B. 2011;115(44):12930–46. https://doi.org/10.1021/jp208796b
15. Yun YH, Bray PJ. Nuclear magnetic resonance studies of the glasses in the system Na_2O-B_2O_3-SiO_2. J Non-Cryst Solids. 1978;27(3):363–80. https://doi.org/10.1016/0022-3093(78)90020-0
16. Ferlat G, Charpentier T, Seitsonen AP, Takada A, Lazzeri M, Cormier L, et al. Boroxol rings in liquid and vitreous B_2O_3 from first principles. Phys Rev Lett. 2008;101(6):065504. https://doi.org/10.1103/PhysRevLett.101.065504
17. Soules TF, Varshneya AK. Molecular dynamic calculations of a sodium borosilicate glass structure. J Am Ceram Soc. 1981;64(3):145–50. https://doi.org/10.1111/j.1151-2916.1981.tb10246.x
18. Meera BN, Ramakrishna J. Raman spectral studies of borate glasses. J Non-Cryst Solids. 1993;159(1):1–21. https://doi.org/10.1016/0022-3093(93)91277-A
19. Bisbrouck N, Bertani M, Angeli F, Charpentier T, de Ligny D, Delaye JM, et al. Impact of magnesium on the structure of aluminoborosilicate glasses: a solid-state NMR and Raman spectroscopy study. J Am Ceram Soc. 2021;104(9):4518–36. https://doi.org/10.1111/jace.17876
20. Dell WJ, Bray PJ, Xiao SZ. ^{11}B NMR studies and structural modeling of Na_2O-B_2O_3-SiO_2 glasses of high soda content. J Non-Cryst Solids. 1983;58(1):1–16. https://doi.org/10.1016/0022-3093(83)90097-2
21. Bray PJ. Structural models for borate glasses. J Non-Cryst Solids. 1985;75(1):29–36. https://doi.org/10.1016/0022-3093(85)90198-X
22. Delaye JM, Ghaleb D. Molecular dynamics simulation of SiO_2 + B_2O_3 + Na_2O + ZrO_2 glass. J Non-Cryst Solids. 1996;195(3):239–48. https://doi.org/10.1016/0022-3093(95)00527-7
23. Gou F, Greaves GN, Smith W, Winter R. Molecular dynamics simulation of sodium borosilicate glasses. J Non-Cryst Solids. 2001;293–295:539–46. https://doi.org/10.1016/S0022-3093(01)00775-X
24. Kieu LH, Delaye JM, Cormier L, Stolz C. Development of empirical potentials for sodium borosilicate glass systems. J Non-Cryst Solids. 2011;357(18):3313–21. https://doi.org/10.1016/j.jnoncrysol.2011.05.024
25. Inoue H, Masuno A, Watanabe Y. Modeling of the structure of sodium borosilicate glasses using pair potentials. J Phys

Chem B. 2012;116(40):12325–31. https://doi.org/10.1021/jp3038126

26. Wang M, Anoop Krishnan NM, Wang B, Smedskjaer MM, Mauro JC, Bauchy M. A new transferable interatomic potential for molecular dynamics simulations of borosilicate glasses. J Non-Cryst Solids. 2018;498:294–304. https://doi.org/10.1016/j.jnoncrysol.2018.04.063
27. Deng L, Du J. Development of boron oxide potentials for computer simulations of multicomponent oxide glasses. J Am Ceram Soc. 2018;105(5):2482–505. https://doi.org/10.1111/jace.16082
28. Sundararaman S, Huang L, Ispas S, Kob W. New interaction potentials for borate glasses with mixed network formers. J Chem Phys. 2020;152(10):104501. https://doi.org/10.1063/1.5142605
29. Shih YT, Sundararaman S, Ispas S, Huang L. New interaction potentials for alkaline earth silicate and borate glasses. J Non-Cryst Solids. 2021;565:120853. https://doi.org/10.1016/j.jnoncrysol.2021.120853
30. Stevensson B, Yu Y, Edén M. Structure–composition trends in multicomponent borosilicate-based glasses deduced from molecular dynamics simulations with improved B–O and P–O force fields. Phys Chem Chem Phys. 2018;20(12):8192–209. https://doi.org/10.1039/C7CP08593A
31. Pacaud F, Delaye JM, Charpentier T, Cormier L, Salanne M. Structural study of Na_2O–B_2O_3 –SiO_2 glasses from molecular simulations using a polarizable force field. J Chem Phys. 2017;147(16):161711. https://doi.org/10.1063/1.4992799
32. Dick BG, Overhauser AW. Theory of the dielectric constants of alkali halide crystals. Phys Rev. 1958;112(1):90–103. https://doi.org/10.1103/PhysRev.112.90
33. Aguado A, Bernasconi L, Madden PA. Interionic potentials from *ab initio* molecular dynamics: the alkaline earth oxides CaO, SrO, and BaO. J Chem Phys. 2003;118(13):5704–17. https://doi.org/10.1063/1.1556074
34. Tuheen MI, Deng L, Du J. A comparative study of the effectiveness of empirical potentials for molecular dynamics simulations of borosilicate glasses. J Non-Cryst Solids. 2021;553:120413. https://doi.org/10.1016/j.jnoncrysol.2020.120413
35. Fortino M, Berselli A, Stone-Weiss N, Deng L, Goel A, Du J, et al. Assessment of interatomic parameters for the reproduction of borosilicate glass structures via DFT-GIPAW calculations. J Am Ceram Soc. 2019;102(12):7225–43. https://doi.org/10.1111/jace.16655
36. Bertani M, Menziani MC, Pedone A. Improved empirical force field for multicomponent oxide glasses and crystals. Phys Rev Mater. 2021;5(4):045602. https://doi.org/10.1103/PhysRevMaterials.5.045602
37. Malavasi G, Pedone A. The effect of the incorporation of catalase mimetic activity cations on the structural, thermal and chemical durability properties of the 45S5 Bioglass®. Acta Mater. 2022;229:117801. https://doi.org/10.1016/j.actamat.2022.117801
38. Pedone A, Malavasi G, Menziani MC, Cormack AN, Segre U. A new self-consistent empirical interatomic potential model for oxides, silicates, and silica-based glasses. J Phys Chem B. 2006;110(24):11780–95. https://doi.org/10.1021/jp0611018
39. Pedone A. Properties calculations of silica-based glasses by atomistic simulations techniques: a review. J Phys Chem C. 2009;113(49):20773–84. https://doi.org/10.1021/jp9071263
40. Afify ND, Mountjoy G. Molecular-dynamics modeling of Eu^{3+}-ion clustering in SiO_2 glass. Phys Rev B. 2009;79(2):024202. https://doi.org/10.1103/PhysRevB.79.024202
41. Al-Hasni BM, Mountjoy G. A molecular dynamics study of the atomic structure of x(MgO) 100−x(SiO_2). J Non-Cryst Solids. 2014;400:33–44. https://doi.org/10.1016/j.jnoncrysol.2013.11.011
42. Angeli F, Villain O, Schuller S, Ispas S, Charpentier T. Insight into sodium silicate glass structural organization by multinuclear NMR combined with first-principles calculations. Geochim Cosmochim Acta. 2011;75(9):2453–69. https://doi.org/10.1016/j.gca.2011.02.003
43. Deng Y, Eames C, Chotard JN, Lalère F, Seznec V, Emge S, et al. Structural and mechanistic insights into fast lithium-ion conduction in Li_4SiO_4 –Li_3PO_4 solid electrolytes. J Am Chem Soc. 2015;137(28):9136–45. https://doi.org/10.1021/jacs.5b04444
44. Konstantinou K, Sushko PV, Duffy DM. Structure and ionic diffusion of alkaline-earth ions in mixed cation glasses A_2O–2MO–4SiO_2 with molecular dynamics simulations. J Non-Cryst Solids. 2015;422:57–63. https://doi.org/10.1016/j.jnoncrysol.2015.05.005
45. Mongalo L, Lopis AS, Venter GA. Molecular dynamics simulations of the structural properties and electrical conductivities of CaO–MgO–Al_2O_3–SiO_2 melts. J Non-Cryst Solids. 2016;452:194–202. https://doi.org/10.1016/j.jnoncrysol.2016.08.042
46. Prasada Rao R, Tho TD, Adams S. Ion transport pathways in molecular dynamics simulated lithium silicate glasses. Solid State Ionics. 2010;181(1–2):1–6. https://doi.org/10.1016/j.ssi.2009.12.003
47. Sadat MR, Bringuier S, Muralidharan K, Runge K, Asaduzzaman A, Zhang L. An atomistic characterization of the interplay between composition, structure and mechanical properties of amorphous geopolymer binders. J Non-Cryst Solids. 2016;434:53–61. https://doi.org/10.1016/j.jnoncrysol.2015.11.022
48. Skinner LB, Barnes AC, Salmon PS, Hennet L, Fischer HE, Benmore CJ, et al. Joint diffraction and modeling approach to the structure of liquid alumina. Phys Rev B. 2013;87(2):024201. https://doi.org/10.1103/PhysRevB.87.024201
49. Tandia A, Vargheese KD, Mauro JC. Elasticity of ion stuffing in chemically strengthened glass. J Non-Cryst Solids. 2012;358(12–13):1569–74. https://doi.org/10.1016/j.jnoncrysol.2012.04.021
50. Urata S, Sato Y. A study on the plasticity of soda-lime silica glass via molecular dynamics simulations. J Chem Phys. 2017;147(17):174501. https://doi.org/10.1063/1.4997293
51. Wood SM, Eames C, Kendrick E, Islam MS. Sodium ion diffusion and voltage trends in phosphates $Na_4M_3(PO_4)_2P_2O_7$ (M = Fe, Mn, Co, Ni) for possible high-rate cathodes. J Phys Chem C. 2015;119(28):15935–41. https://doi.org/10.1021/acs.jpcc.5b04648
52. Pedone A, Malavasi G, Cormack AN, Segre U, Menziani MC. Insight into elastic properties of binary alkali silicate glasses; prediction and interpretation through atomistic simulation techniques. Chem Mater. 2007;19(13):3144–54. https://doi.org/10.1021/cm062619r
53. Pedone A, Malavasi G, Menziani MC, Segre U, Cormack AN. Molecular dynamics studies of stress−strain behavior of silica glass under a tensile load. Chem Mater. 2008;20(13):4356–66. https://doi.org/10.1021/cm800413v
54. Pedone A, Menziani MC, Cormack AN. Dynamics of fracture in silica and soda-silicate glasses: from bulk materials to

nanowires. J Phys Chem C. 2015;119(45):25499–507. https://doi.org/10.1021/acs.jpcc.5b08657
55. Pedone A, Malavasi G, Cormack AN, Segre U, Menziani MC. Elastic and dynamical properties of alkali-silicate glasses from computer simulations techniques. Theor Chem Acc. 2008;120(4–6):557–64. https://doi.org/10.1007/s00214-008-0434-7
56. Smith W, Forester TR. DL_POLY_2.0: a general-purpose parallel molecular dynamics simulation package. J Mol Graphics. 1996;14(3):136–41. https://doi.org/10.1016/S0263-7855(96)00043-4
57. Deng L, Du J. Effects of system size and cooling rate on the structure and properties of sodium borosilicate glasses from molecular dynamics simulations. J Chem Phys. 2018;148(2):024504. https://doi.org/10.1063/1.5007083
58. Allen MP, Tildesley DJ. Computer Simulation of Liquids. 2nd ed. Oxford: Oxford University Press; 2017. http://doi.org/10.1093/oso/9780198803195.001.0001
59. Lee H, Cai W. Ewald summation for coulomb interactions in a periodic supercell. Lecture notes. Redwood City, California: Stanford University; 2009.
60. Gale JD. Empirical potential derivation for ionic materials. Philos Mag B. 1996;73(1):3–19. https://doi.org/10.1080/13642819608239107
61. Gale JD, Rohl AL. The general utility lattice program (GULP). Mol Simul. 2003;29(5):291–341. https://doi.org/10.1080/0892702031000104887
62. Fang SM. The crystal structure of sodium metaborate $Na_3(B_3O_6)$. Z Kristallogr – Cryst Mater. 1938;99(1–6):1–8. https://doi.org/10.1524/zkri.1938.99.1.1
63. Gurr GE, Montgomery PW, Knutson CD, Gorres BT. The crystal structure of trigonal diboron trioxide. Acta Crystallogr B. 1970;26(7):906–15. https://doi.org/10.1107/S0567740870003369
64. Vegas A, Cano FH, García-Blanco S. The crystal structure of calcium orthoborate: a redetermination. Acta Crystallogr B. 1975;31(5):1416–9. https://doi.org/10.1107/S0567740875005316
65. Marezio M, Remeika JP. Polymorphism of $LiMO_2$ compounds and high-pressure single-crystal synthesis of $LiBO_2$. J Chem Phys. 1966;44(9):3348–53. https://doi.org/10.1063/1.1727236
66. Shepelev YuF, Bubnova RS, Filatov SK, Sennova NA, Pilneva NA. LiB_3O_5 crystal structure at 20, 227 and 377°C. J Solid State Chem. 2005;178(10):2987–97. https://doi.org/10.1016/j.jssc.2005.06.017
67. Guo GC, Cheng WD, Chen JT, Zhuang HH, Huang JS, Zhang QE. Monoclinic $Mg_2B_2O_5$. Acta Crystallogr C. 1995;51(12):2469–71. https://doi.org/10.1107/S0108270195008298
68. Appleman DE, Clark JR. Crystal structure of reedmergnerite, a boron albite, and its relation to feldspar crystal chemistry. Am Mineral. 1965;50:1827–50.
69. Sokolova EV, Hawthorne FC, Khomyakov AP. The crystal chemistry of malinkoite, $NaBSiO_4$, and lisitsynite, $KBSi_2O_6$, from the Khibina Lovozero complex, Kola peninsula, Russia. Can Mineral. 2001;39(1):159–69. https://doi.org/10.2113/gscanmin.39.1.159
70. Pauling L. The nature of the chemical bond. Application of results obtained from the quantum mechanics and from a theory of paramagnetic susceptibility to the structure of molecules. J Am Chem Soc. 1931;53(4):1367–400. https://doi.org/10.1021/ja01355a027
71. Noritake F, Kawamura K. The nature of Si-O-Si bonding via molecular orbital calculations. J Comput Chem Jpn. 2015;14(4):124–30. https://doi.org/10.2477/jccj.2015-0009
72. van Duin ACT, Strachan A, Stewman S, Zhang Q, Xu X, Goddard WA. ReaxFFSiO reactive force field for silicon and silicon oxide systems. J Phys Chem A. 2003;107(19):3803–11. https://doi.org/10.1021/jp0276303
73. Antony J. 6 – Full factorial designs. In: Antony J, editor. Des. Exp. Eng. Sci. 2nd ed. Oxford: Elsevier; 2014. p. 63–85. https://doi.org/10.1016/B978-0-08-099417-8.00006-7
74. Lundstedt T, Seifert E, Abramo L, Thelin B, Nyström Å, Pettersen J, et al. Experimental design and optimization. Chemom Intell Lab Syst. 1998;42(1):3–40. https://doi.org/10.1016/S0169-7439(98)00065-3
75. Wagner JR, Mount EM, Giles HF. 25 – Design of experiments. In: Wagner JR, Mount EM, Giles HF, editors. Extrusion. 2nd ed. Oxford: William Andrew Publishing; 2014. p. 291–308. https://doi.org/10.1016/B978-1-4377-3481-2.00025-9
76. Antony J. 4 – A systematic methodology for design of experiments. In: Antony J, editor. Des. Exp. Eng. Sci. 2nd ed. Oxford: Elsevier; 2014. p. 33–50. https://doi.org/10.1016/B978-0-08-099417-8.00004-3
77. Brochu E, Cora VM, de Freitas N. A tutorial on bayesian optimization of expensive cost functions, with application to active user modeling and hierarchical reinforcement learning. 2010. ArXiv, abs/1012.2599. https://doi.org/10.48550/arXiv.1012.2599
78. Liu H, Fu Z, Li Y, Sabri NFA, Bauchy M. Parameterization of empirical forcefields for glassy silica using machine learning. MRS Commun. 2019;9:593–9. https://doi.org/10.1557/mrc.2019.47
79. Rasmussen CE, Williams CKI. Gaussian processes for Machine learning (adaptive computation and machine learning). Broadway, Cambridge: The MIT Press; 2005
80. Nugueira F. Bayesian optimization: open source constrained global optimization tool for Python. 2014. https://github.com/fmfn/BayesianOptimization
81. Snoek J, Larochelle H, Adams RP. Practical bayesian optimization of machine learning algorithms. In: Pereira F, Burges CJ, Bottou L, Weinberger KQ, editors. Adv. Neural Inf. Process. Syst. vol 25. New York: Curran Associates, Inc.; 2012.
82. Srinivas N, Krause A, Kakade S, Seeger M. Gaussian process optimization in the bandit setting: no regret and experimental design. Proc. 27th Int. Conf. Int. Conf. Mach. Learn. Madison, WI, USA: Omnipress; 2010. p. 1015–1022.
83. Pedesseau L, Ispas S, Kob W. First-principles study of a sodium borosilicate glass-former. II. The glass state. Phys Rev B. 2015;91(13):134202. https://doi.org/10.1103/PhysRevB.91.134202
84. Pedesseau L, Ispas S, Kob W. First-principles study of a sodium borosilicate glass-former. I. The liquid state. Phys Rev B. 2015;91(13):134201. https://doi.org/10.1103/PhysRevB.91.134201
85. Horiuchi H, Hirano M, Ito E, Matsui Y. $MgSiO_3$ (ilmenite-type): single crystal X-ray diffraction study. Am Mineral. 1982;67(7–8):788–93.
86. Fiquet G, Dewaele A, Andrault D, Kunz M, Le Bihan T. Thermoelastic properties and crystal structure of $MgSiO_3$ perovskite at lower mantle pressure and temperature conditions. Geophys Res Lett. 2000;27(1):21–4. https://doi.org/10.1029/1999GL008397

87. Takéuchi Y. The crystal structure of magnesium pyroborate. Acta Crystallogr. 1952;5(5):574–81. https://doi.org/10.1107/S0365110x52001623
88. Sørensen SS, Johra H, Mauro JC, Bauchy M, Smedskjaer MM. Boron anomaly in the thermal conductivity of lithium borate glasses. Phys Rev Mater. 2019;3(7):075601. https://doi.org/10.1103/PhysRevMaterials.3.075601
89. Doweidar H. Consideration of the boron oxide anomaly. J Mater Sci. 1990;25(1):253–8. https://doi.org/10.1007/BF00544216
90. Gaafar MS, Marzouk SY, Zayed HA, Soliman LI, Serag El-Deen AH. Structural studies and mechanical properties of some borate glasses doped with different alkali and cobalt oxides. Curr Appl Phys. 2013;13(1):152–8. https://doi.org/10.1016/j.cap.2012.07.007
91. Yiannopoulos YD, Chryssikos GD, Kamitsos EI. Structure and properties of alkaline earth borate glasses. Phys Chem Glass. 2001;42(3):164–72.
92. Wu J, Stebbins JF. Cation field strength effects on boron coordination in binary borate glasses. J Am Ceram Soc. 2014;97(9):2794–801. https://doi.org/10.1111/jace.13100
93. Michaelis VK, Aguiar PM, Kroeker S. Probing alkali coordination environments in alkali borate glasses by multinuclear magnetic resonance. J Non-Cryst Solids. 2007;353(26):2582–90. https://doi.org/10.1016/j.jnoncrysol.2007.04.029
94. Zhong J, Bray PJ. Change in boron coordination in alkali borate glasses, and mixed alkali effects, as elucidated by NMR. J Non-Cryst Solids. 1989;111(1):67–76. https://doi.org/10.1016/0022-3093(89)90425-0
95. Budhwani KI, Feller S. A density model for the lithium, sodium and potassium borosilicate glass systems. Phys Chem Glasses. 1995;36:183–90
96. Takahashi K, Osaka A, Furuno R. The elastic properties of the glasses in the systems R_2O-B_2O_3-SiO_2 (R = Na and K) and Na_2O-B_2O_3. J Ceram Assoc Jpn. 1983;91(5):199–205.
97. Barlet M, Delaye JM, Charpentier T, Gennisson M, Bonamy D, Rouxel T, et al. Hardness and toughness of sodium borosilicate glasses via Vickers's indentations. J Non-Cryst Solids. 2015;417–418:66–79. https://doi.org/10.1016/j.jnoncrysol.2015.02.005
98. Shibata M, Sanchez C, Patel H, Feller S, Stark J, Sumcad G, et al. The density of lithium borate glasses related to atomic arrangements. J Non-Cryst Solids. 1986;85(1):29–41. https://doi.org/10.1016/0022-3093(86)90076-1
99. Kodama M, Kojima S. Velocity of sound in and elastic properties of alkali metal borate glasses. Phys Chem Glass: Eur J Glass Sci Technol Part B. 2014;55(1):1–12.
100. Lower NP, McRae JL, Feller HA, Betzen AR, Kapoor S, Affatigato M, et al. Physical properties of alkaline-earth and alkali borate glasses prepared over an extended range of compositions. J Non-Cryst Solids. 2001;293–295:669–75.
101. Wright A, Sinclair R, Stone C, Shaw J, Feller S, Kiczenski T, et al. A neutron diffraction study of $2M_2O.5B_2O_3$ (M = Li, Na, K, Rb, Cs & Ag) and $2MO.5B_2O_3$ (M = Ca & Ba) glasses. Eur J Glass Sci Technol Part B Phys Chem Glass. 2012;53:191–204.
102. Wright A, Sinclair R, Stone C, Shaw J, Feller S, Williams R, et al. A neutron diffraction study of sodium, rubidium and cæsium borate glasses. Phys Chem Glass: Eur J Glass Sci Technol Part B. 2014;55: 74-84.
103. Krogh-Moe J. The structure of vitreous and liquid boron oxide. J Non-Cryst Solids. 1969;1(4):269–84. https://doi.org/10.1016/0022-3093(69)90025-8
104. Wright AC. Neutron and X-ray amorphography. J Non-Cryst Solids. 1988;106(1):1–16. https://doi.org/10.1016/0022-3093(88)90218-9
105. Wright AC. The comparison of molecular dynamics simulations with diffraction experiments. J Non-Cryst Solids. 1993;159(3):264–68. https://doi.org/10.1016/0022-3093(93)90232-M
106. Stebbins JF, Zhao P, Kroeker S. Non-bridging oxygens in borate glasses: characterization by ^{11}B and ^{17}O MAS and 3QMAS NMR. Solid State Nucl Magn Reson. 2000;16(1–2):9–19. https://doi.org/10.1016/s0926-2040(00)00050-3
107. Montouillout V, Fan H, del Campo L, Ory S, Rakhmatullin A, Fayon F, et al. Ionic conductivity of lithium borate glasses and local structure probed by high resolution solid-sate NMR. J Non-Cryst Solids. 2018;484:57–64. https://doi.org/10.1016/j.jnoncrysol.2018.01.020
108. Maekawa H, Maekawa T, Kawamura K, Yokokawa T. The structural groups of alkali silicate glasses determined from ^{29}Si MAS-NMR. J Non-Cryst Solids. 1991;127(1):53–64. https://doi.org/10.1016/0022-3093(91)90400-Z
109. Murdoch JB, Stebbins JF, Carmichael ISE. High-resolution ^{29}Si NMR study of silicate and aluminosilicate glasses: the effect of network-modifying cations. Am Mineral. 1985;70(3–4):332–43.
110. Magi M, Lippmaa E, Samoson A, Engelhardt G, Grimmer AR. Solid-state high-resolution silicon-29 chemical shifts in silicates. J Phys Chem. 1984;88(8):1518–22. https://doi.org/10.1021/j150652a015
111. Nanba T, Nishimura M, Miura Y. A theoretical interpretation of the chemical shift of ^{29}Si NMR peaks in alkali borosilicate glasses. Geochim Cosmochim Acta. 2004;68(24):5103–11. https://doi.org/10.1016/j.gca.2004.05.042
112. Pedone A, Charpentier T, Malavasi G, Menziani MC. New insights into the atomic structure of 45S5 bioglass by means of solid-state NMR spectroscopy and accurate first-principles simulations. Chem Mater. 2010;22(19):5644–52. https://doi.org/10.1021/cm102089c

SUPPORTING INFORMATION

Additional supporting information can be found online in the Supporting Information section at the end of this article.

How to cite this article: Bertani M, Pallini A, Cocchi M, Menziani MC, Pedone A. A new self-consistent empirical potential model for multicomponent borate and borosilicate glasses. J Am Ceram Soc. 2022;105:7254–7271. https://doi.org/10.1111/jace.18681